

## Article

# Investigation of Composite Structure with Dual Fabry–Perot Cavities for Temperature and Pressure Sensing

Jun Wang <sup>1</sup>, Long Li <sup>1</sup>, Shuaicheng Liu <sup>1</sup>, Diyang Wu <sup>1</sup>, Wei Wang <sup>1,2</sup>, Ming Song <sup>1</sup>, Guanjun Wang <sup>1,2,3,\*</sup> and Mengxing Huang <sup>1,2,\*</sup>

- <sup>1</sup> School of Information and Communication Engineering, Hainan University, Haikou 570228, China; 20180581310080@hainanu.edu.cn (J.W.); 20181683310167@hainanu.edu.cn (L.L.); 20181683310012@hainanu.edu.cn (S.L.); 20181683310111@hainanu.edu.cn (D.W.); 20081000110002@hainanu.edu.cn (W.W.); 20171683310058@hainanu.edu.cn (M.S.)
- <sup>2</sup> State Key Laboratory of Marine Resource Utilization in South China Sea, Hainan University, Haikou 570228, China
- <sup>3</sup> Wuhan National Laboratory for Optoelectronics, Huazhong University of Science and Technology, Wuhan 430074, China
- \* Correspondence: wangguanjun@hainanu.edu.cn (G.W.); huangmx09@hainanu.edu.cn (M.H.)

**Abstract:** To deeply analyze the influence of diaphragm materials on the temperature and pressure sensitivity of Fabry–Perot interferometer-based dual-parameter fiber sensors, the multiple transfer method was used to fabricate the dual Fabry–Perot cavities, respectively, consisting of the following combinations: epoxy resin AB/polydimethylsiloxane (PDMS), Ecoflex0030 silicone rubber /PDMS, and PDMS/Ecoflex0030 silicone rubber. Experimental results show that the temperature sensitivities are, respectively, 528, 540, and 1033 pm/°C in the range of 40–100 °C. Within the applied pressure range of 100–400 kPa, the pressure sensitivities are, respectively, 16.0, 34.6, and 30.2 pm/kPa. The proposed sensors have advantages of proper sensitivity, simple fabrication, cost-effectiveness, controllable cavity length, and suitability for practical sensing applications.



**Citation:** Wang, J.; Li, L.; Liu, S.; Wu, D.; Wang, W.; Song, M.; Wang, G.; Huang, M. Investigation of Composite Structure with Dual Fabry–Perot Cavities for Temperature and Pressure Sensing. *Photonics* **2021**, *8*, 138. <https://doi.org/10.3390/photonics8050138>

Received: 24 February 2021

Accepted: 9 April 2021

Published: 23 April 2021

**Publisher's Note:** MDPI stays neutral with regard to jurisdictional claims in published maps and institutional affiliations.



**Copyright:** © 2021 by the authors. Licensee MDPI, Basel, Switzerland. This article is an open access article distributed under the terms and conditions of the Creative Commons Attribution (CC BY) license (<https://creativecommons.org/licenses/by/4.0/>).

**Keywords:** Fabry–Perot cavity; temperature/pressure sensing; composite structure; multiple transfer method

## 1. Introduction

Optical fiber sensors have been widely used in many domains owing to the advantages of low cost, high sensitivity, fast response time, and good stability. Simultaneously, different sensor structures with diverse sensitivities to various parameters can be used to realize dual- or even multi-parameter sensing, such as temperature, pressure, refractive index, etc. [1,2].

Several studies have characterized the investigations of single or dual-parameter monitoring based on fiber tip bubble [3], Mach–Zehnder interferometer [4], fiber Bragg gratings [5], Sagnac interferometer [6], etc. Due to the advantages of small size, good measurement performance, and survivability in complicated electromagnetic environment [7–19], Fabry–Perot Interferometer (FPI)-based dual-parameter fiber sensors have been extensively studied for the measurement of temperature and pressure. However, FPI-based fiber sensors impose the limitation of the durability and operation stability of the thin diaphragm that is used to form the FP cavity. Consequently, series of dual FP cavities sensors based on various diaphragms to improve the sensing performance are utilized to monitor the temperature and pressure [7–12], which share the characteristic of ultra-high sensitivity. While endlessly pursuing high sensitivity will bring several problems which should be paid more attention, only this kind of fiber sensor can be applied for ultra-precise monitoring applications. Moreover, it will result in a great challenge for the design of the interrogator's bandwidth. Another dual FPI-based fiber sensor consisting of two tiny segments of hollow-core fiber located at the end of lead-in single mode fiber,

with a misalignment fusion splicing between the two hollow-core fibers with different core diameter, is reported in [13]. The proposed sensor can be used in simultaneous measurement of pressure and temperature, but its sensitivity should be significantly enhanced. Some chemical etching method-assisted FPI fabrication processes are reported in [14–16], which can provide good sensing performances. Unfortunately, the corrosive effects of the chemical etching and the precise etching time are difficult to control. The authors of [17,18] demonstrated easy-to-fabricate dual-FPIs. However, the sensitivity and repeatability of the fabrication for the FP cavity should be improved. By filling a hollow capillary with two sections of PDMS, which are fused to the single-mode fiber, the authors of [19] investigated a novel dual FP cavities-based fiber sensor to detect the temperature and pressure. However, the fabrication of this kind of structure is costly due to the fact an especially made capillary cone is required to inject the PDMS into the hollow capillary.

Although many studies reported dual-parameter monitoring based on FPI structures, it is still worth continuously investigating and demonstrating the design of sensor structures, the selection of sensor materials, and the optimization of fabrication processes. Hence, in this paper, a novel FP cavity with composite structure for fiber sensing based on the multiple transfer method is proposed to measure the temperature and pressure, which possesses the advantages of proper sensitivity, simple fabrication, cost-effectiveness, and controllable cavity length.

## 2. Sensing Principle and Fabrication Process

### 2.1. Sensing Principle

The composite structure with dual FP cavities studied in this paper is depicted in Figure 1. The sensor consists of a single mode fiber tail and two diaphragms with different materials.

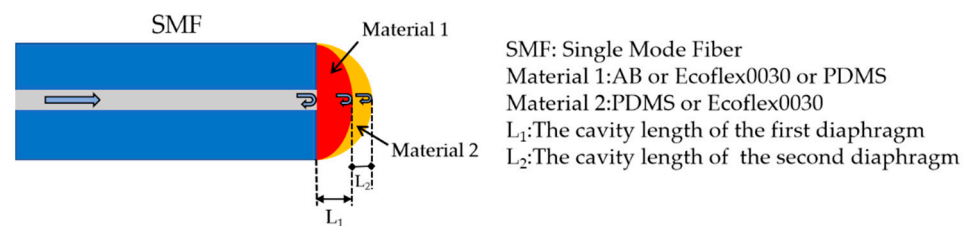


Figure 1. The composite structure based on dual FP cavities.

The formed structure is composed of three reflective surfaces. The interfaces of SMF/Material 1, Material 1/Material 2, Material 2/air, respectively, are reflective surfaces 1, 2 and 3. When light reaches the end face of the optical fiber, the incident light will be reflected by the reflective surface within a certain wavelength range. However, part of the light will still pass through Reflective Surface 1 and be reflected by Reflective Surfaces 2 and 3 within a certain range. The interference spectrum results from the phase delay caused by optical path difference and the different reflectivity of each reflection surface of the composite structure, as

$$I = I_1 + I_2 + 2\sqrt{I_1 I_2} \cos\left(\frac{4\pi nL}{\lambda} + \varphi_0\right) \tag{1}$$

Formula (1) is the dual-beam interference model of the single FP cavity.  $I_1$  and  $I_2$  represent the reflected light intensity of the two-beam interference,  $\lambda$  is the wavelength of the incident light,  $n$  is the refractive index of the FP cavity,  $L$  is the length between two reflected surfaces, and  $\varphi_0$  is the initial phase of the inference.

In this paper, an improved three-beam interference model based on the sensor structure is presented and analyzed. According to the principle of multi-beam interference, the corresponding three-beam interference intensity [20] can be described as

$$I = I_1 + I_2 + I_3 - 2\sqrt{I_1 I_2} \cos\left(\frac{4\pi}{\lambda} n_1 L_1 + \varphi_1\right) + 2\sqrt{I_2 I_3} \cos\left(\frac{4\pi}{\lambda} n_2 L_2 + \varphi_2\right) - 2\sqrt{I_1 I_2} \cos\left(\frac{4\pi}{\lambda} (n_1 L_1 + n_2 L_2) + \varphi_3\right) \tag{2}$$

where  $I_1$ ,  $I_2$ , and  $I_3$ , respectively, are the reflected light intensity at the three reflecting surfaces;  $\varphi_1$ ,  $\varphi_2$ , and  $\varphi_3$  are the initial phases of the reflected light; and  $n_1$  and  $n_2$  are the refractive index of Material 1 and Material 2, respectively.

$$L = \lambda_1 \cdot \frac{\lambda_2}{2(\lambda_2 - \lambda_1)} \tag{3}$$

where  $\lambda_1$ ,  $\lambda_2$  are the wavelengths corresponding to the adjacent peaks or valleys in the temperature and pressure test interference spectrum, and  $L$  is the length of FP cavity.

The optical path difference (OPD) of the reflected light  $l$  can be expressed as

$$l = 2nL \tag{4}$$

The wavelength spacing between adjacent peaks or valleys of the sensor interference spectrum is the free spectral range (FSR), the FSR is expressed as

$$FSR = \frac{\lambda_1 \lambda_2}{2nL} = \frac{\lambda_0^2}{2nL} \tag{5}$$

where the  $\lambda_1$  and  $\lambda_2$  are two adjacent peaks or valleys of the interference spectrum,  $\lambda_0$  is the mean wavelength of  $\lambda_1$  and  $\lambda_2$ , and  $L$  corresponds to the cavity length in formula (3). The FSR is mainly affected by the thermal expansion coefficient (which is related to the change of  $L$ ) and the thermo-optic coefficient (which is related to the change of  $n$ ). It can be clearly seen that the FSR of the interference spectrum decreases as the  $n$  and  $L$  increase.

For the temperature/pressure measurement of the FPI-based fiber sensor, the response of the sensor can be attributed to thermal expansion effects, thermo-optic effects, elastic deformation effects and refractive index factors. During temperature measurement, the refractive index and cavity length of the FP cavity change as the temperature increases, since these are related to the thermo-optical coefficient and the thermal expansion coefficient, respectively. This results in the variations of OPD. The OPD variation is defined as [21]

$$\begin{cases} \Delta l = 2\Delta nL + 2n\Delta L = 2nL(\delta + \alpha)\Delta T \\ \Delta n = \delta\Delta Tn \\ \Delta L = \alpha\Delta TL \end{cases} \tag{6}$$

where  $\Delta l$ ,  $\Delta T$ ,  $\Delta n$  and  $\Delta L$  are the variations of OPD, temperature, refractive index and FP cavity length, respectively;  $\delta$  and  $\alpha$  are the thermo-optic coefficient and thermal expansion coefficient, respectively, that are closely related to the properties of diaphragms. The formula (6) indicates that the temperature-induced OPD variations can be expressed as the change of FPI cavity length and refractive index.

For the pressure measurement, the change of FPI cavity length depends on the diaphragm's elastic deformation effects, and Formula (7) shows the pressure sensing principle [22]:

$$\Delta L = \frac{3}{16} \cdot \frac{(1 - \mu^2)r^4}{Eh^3} \Delta P \tag{7}$$

where  $\Delta P$ ,  $h$ ,  $r$ ,  $\mu$  and  $E$ , respectively, are the change of pressure of the test environment, the thickness, the effective radius, Poisson's Ratio, Young's modulus of the diaphragms.

The theoretical interference spectrum is depicted in Figure 2, which is simulated by Matlab platform. It is obtained by comprehensively considering the relevant parameters of the diaphragms, such as thermo-optical coefficient, thermal expansion coefficient, Young's modulus and Poisson's ratio in the proposed formulas.

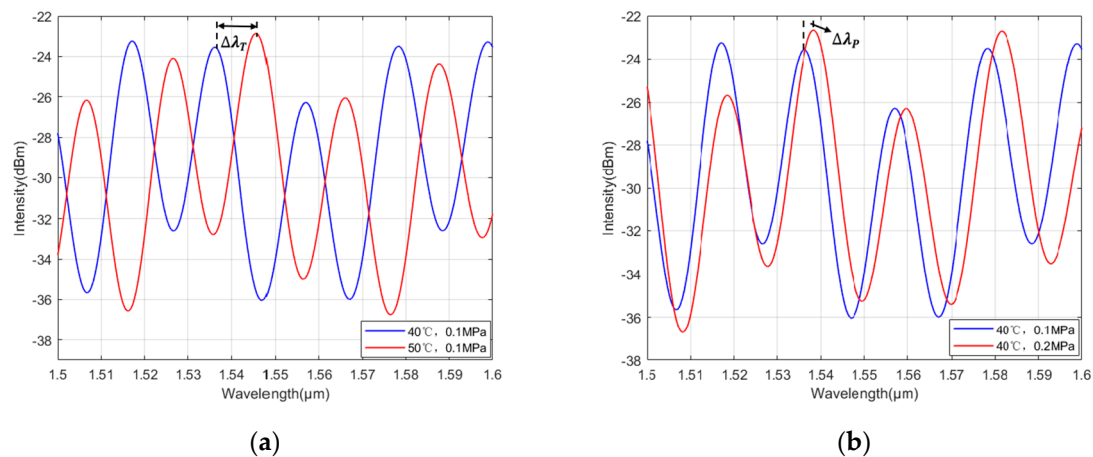


**Figure 2.** (a) The theoretical spectrum of temperature ( $\Delta T = 10\text{ }^\circ\text{C}$ ) response ( $\Delta\lambda_T \approx 10.0\text{ nm}$ ); and (b) the theoretical spectrum of pressure ( $\Delta P \approx 0.1\text{ MPa}$ ) response ( $\Delta\lambda_T \approx 0.9\text{ nm}$ ).

The sensitivity ( $S$ ) of the prepared sensor is defined as the ratio of the wavelength shift over the corresponding temperature or pressure change. Similarly, we define the ratio of the minimum resolution  $\Omega$  ( $\Omega = 20\text{ pm}$ ) of the spectrometer (OSA) over the sensor sensitivity  $S$  as the minimum measurement accuracy ( $MMA$ )—and the  $MMA$  is given by [23]

$$MMA = \frac{\Omega}{S} \tag{8}$$

As Table 1 shows the optic and physical properties of the diaphragms, this paper fully demonstrates the different properties of materials that make up different FP cavities. The thermo-optical coefficient and thermal expansion coefficient are closely related to the temperature effect, which, respectively, affect the refractive index and the cavity length of the diaphragms. Young’s modulus is the modulus of elasticity along the longitudinal direction, which also indicates the rigidity of the material. The lower Young’s modulus induces the greater elastic deformation. Additionally, the tensile strength is similar to Young’s modulus. Poisson’s ratio effectively reflects the elastic constant of material transverse deformation. The pressure sensing characteristics of the sensors mainly rely on the Young’s modulus and Poisson’s ratio of the diaphragms.

**Table 1.** The optic and physical properties of the diaphragms [24–29].

	PDMS	Ecoflex0030 Silicone Rubber	Epoxy Resin AB
Thermo-optic coefficient ( $^\circ\text{C}^{-1}$ )	$-5.0 \times 10^{-4}$	$-3.1 \times 10^{-4}$	$-1.0 \times 10^{-4}$
Thermal expansion coefficient ( $\text{m}/\text{m}^\circ\text{C}$ )	$300 \times 10^{-6}$	$5.9\text{--}7.9 \times 10^{-4}$	$1.948 \times 10^{-6}$
Refractive index (RIU)	1.418	1.41–1.53	1.45–1.52
Young’s modulus (MPa)	5	2	21,250
Poisson’s ratio	0.46	0.369	0.25
Tensile strength (psi)	$1.015 \times 10^3$	200	$1.044 \times 10^4$

### 2.2. Fabrication Process

Figure 3 illustrates the fabrication process that is divided into the five steps: (I) The standard single mode fiber (SMF1) is well cut by a fiber cleaver; (II) PDMS, Ecoflex0030 and epoxy resin AB are prepared and stored at ratios of 10:1, 1:1, and 1:1, respectively. The Material 1 is transferred to SMF2 by the multiple transfers method to form the appropriate diaphragm thickness; (III) The SMF1, SMF2 coated with Material 1 are fixed on the fiber holder. The motor is tuned, which holds SMF2, to coaxially shift the tail of SMF2 to access to the tail of SMF1, before moving it away immediately; (IV) The SMF1 is left standing or heated to make the Material 1 solidified to form the diaphragms. The Material 2 is transferred onto Material 1 by repeating steps (II) and (III); (V) The diaphragms are cured

on SMF1 and a well-fabricated composite structure with dual FP cavities is completed. In addition, the diaphragm thickness can be controlled by increasing or reducing the transfer times. The multiple transfer method can also be used to increase the diaphragm thickness in batches. Consequently, we achieve a controllable cavity length of about 10–30  $\mu\text{m}$ . It can be heated properly to increase the solidification of the diaphragms, which is also helpful to control the cavity length.

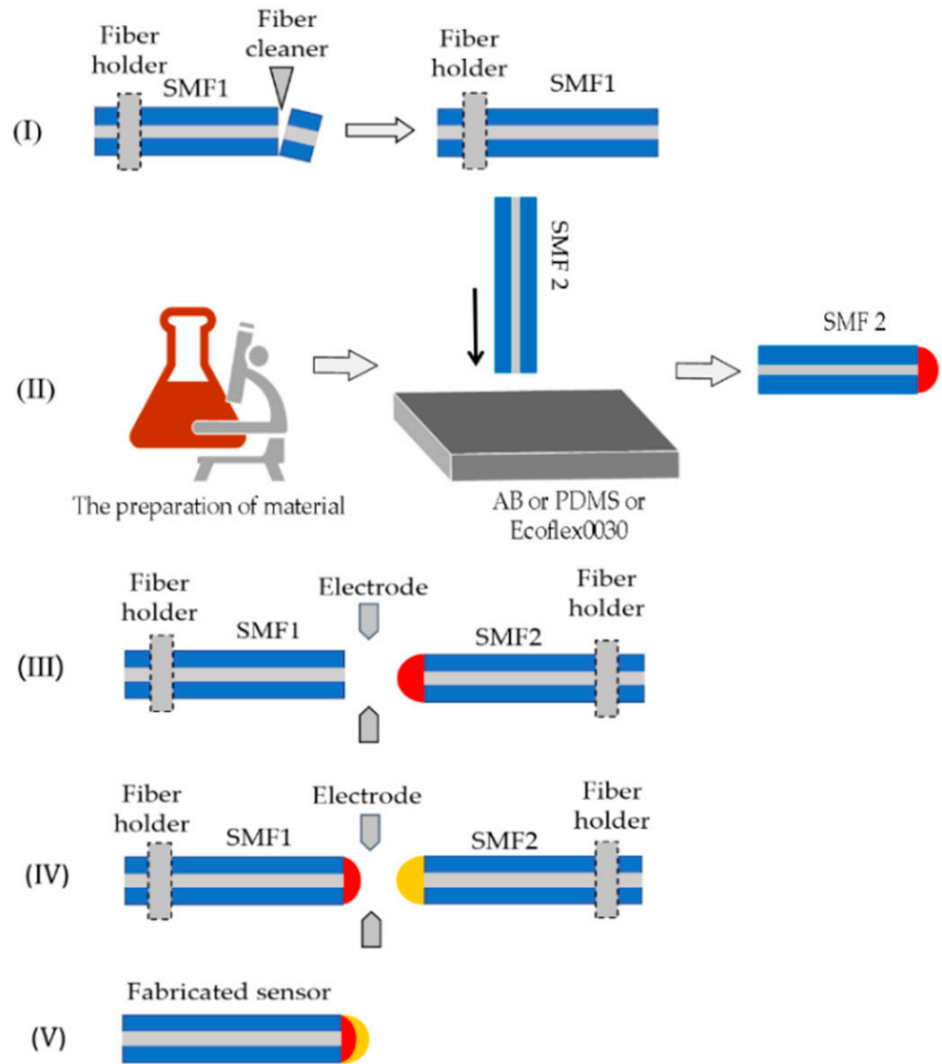


**Figure 3.** The preparation process of the composite structure based on dual FP cavities.

Figure 4a,c demonstrate the interference spectra of a single-cavity structure and a dual-cavity structure ( $S_1$ ) based on the three-beam interference principle. Figure 4a,c can only display the interference spectrum within the range of 1525–1610 nm due to the limited bandwidth of ASE light source. The free spectrum ranges of the sensors are 53 and 27 nm, respectively, owing to the difference of cavity length and refractive index. Simultaneously, different FP cavities have different contributions to the reflected intensity. This can be demonstrated by the fast Fourier transform (FFT) of the total reflected spectrum of the sensor. As shown in Figure 4d, there are two particularly distinct frequency peaks, labeled Peak 1 ( $0.03525 \text{ nm}^{-1}$ ) and Peak 2 ( $0.05875 \text{ nm}^{-1}$ ).

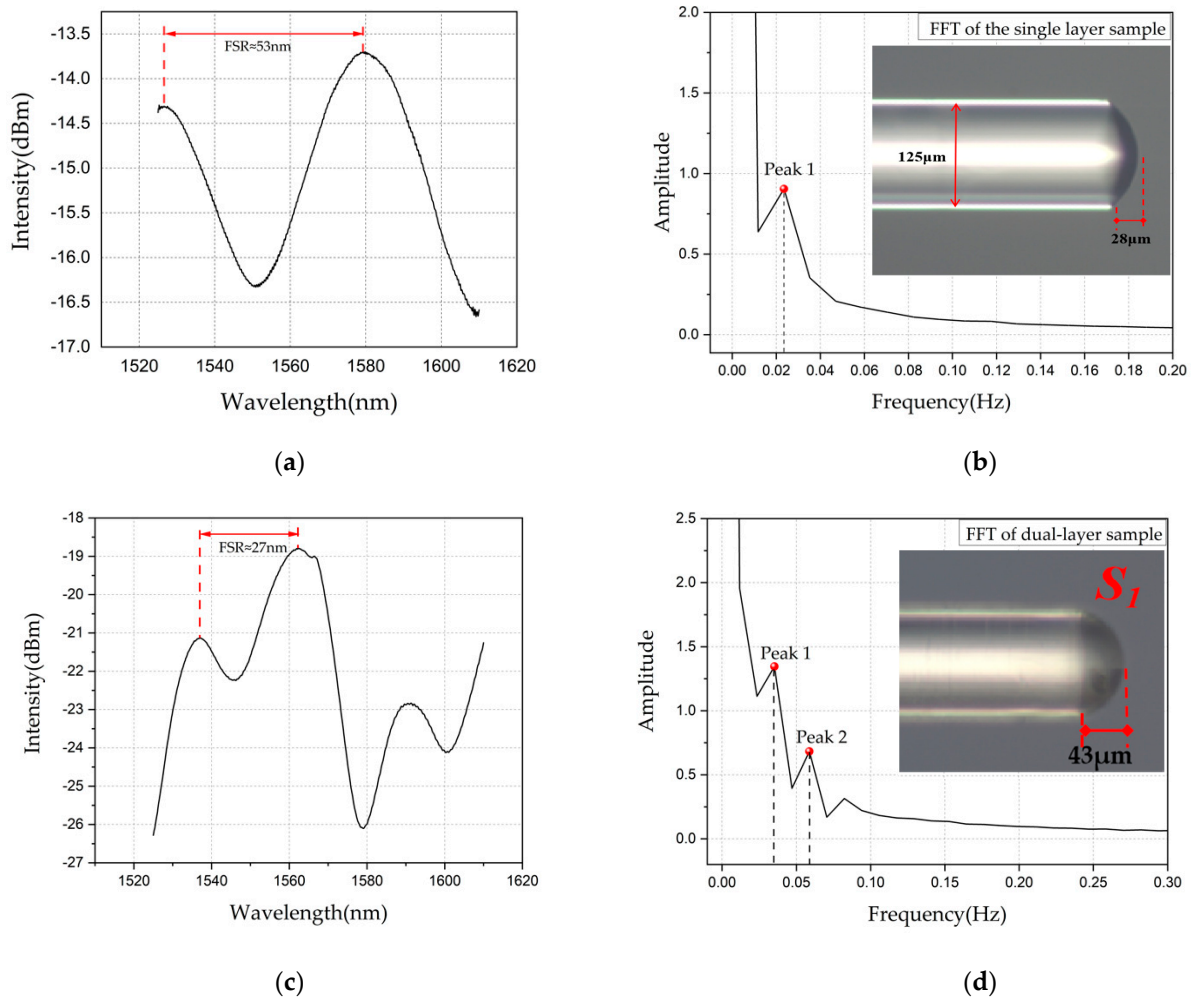


**Figure 4.** Comparison of the fabricated FP sensors: (a) the interference spectrum of a single cavity sensor; (b) the Fourier transform spectrum of Figure 4a; (c) the interference spectrum of a dual cavities sensor  $S_1$ ; and (d) the Fourier transform spectrum of  $S_1$ .

### 3. Experimental Results and Analysis

To ensure the reliability and accuracy of the sensors, this paper carried out a comparative analysis, mainly discussing three types of composite structure, followed by  $S_1$ -Epoxy resin AB/PDMS;  $S_2$ -Ecoflex0030 silicone rubber/PDMS,  $S_3$ -PDMS/Ecoflex0030 silicone rubber. The experimental results showed that the other three composite structures have poor responses to the temperature/pressure. Therefore, they are not discussed in this paper. Table 2 displays the diaphragm thickness of the above three composite ( $S_1$ ,  $S_2$  and  $S_3$ ) for temperature/pressure sensing.

**Table 2.** Diaphragm thickness of each composite structure with different materials.

Composite Structure	Material	Thickness
$S_1$	Material 1: AB	32 $\mu\text{m}$
	Material 2: PDMS	11 $\mu\text{m}$
$S_2$	Material 1: Ecoflex0030	31 $\mu\text{m}$
	Material 2: PDMS	10 $\mu\text{m}$
$S_3$	Material 1: PDMS	28 $\mu\text{m}$
	Material 2: Ecoflex0030	12 $\mu\text{m}$

### 3.1. Temperature Sensitivity Analysis

The three samples were tested by the system shown in Figure 5. The temperature increased from 40 to 150 °C with increments of 10 °C. Meanwhile, the spectrometer persistently monitored the change of interference spectrum. The experimental results demonstrate that the measurement range of  $S_1$  was about 40–120 °C, while  $S_2$  and  $S_3$  have a better temperature response around 40–130 °C, which is related to the unique properties of materials at high temperature. The stable experimental results over the range of 40–100 °C were selected for analysis.

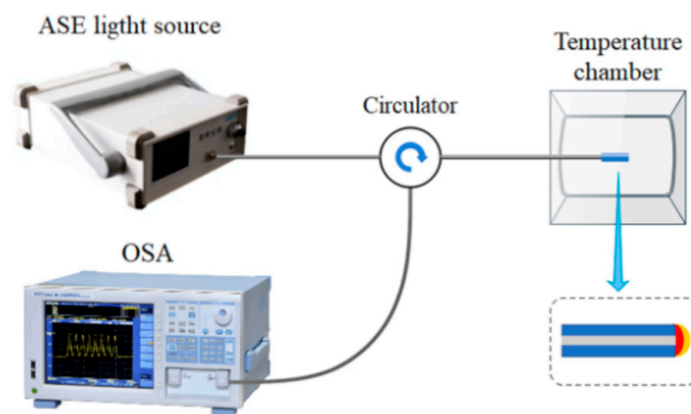
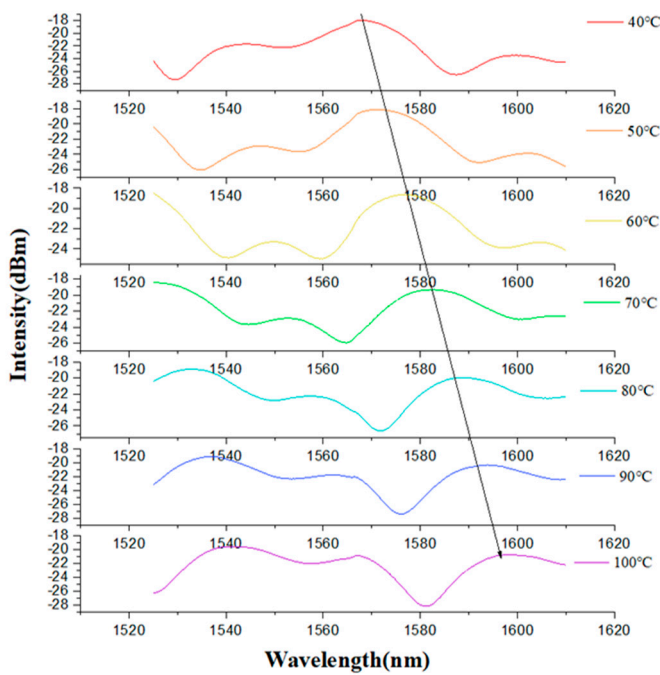
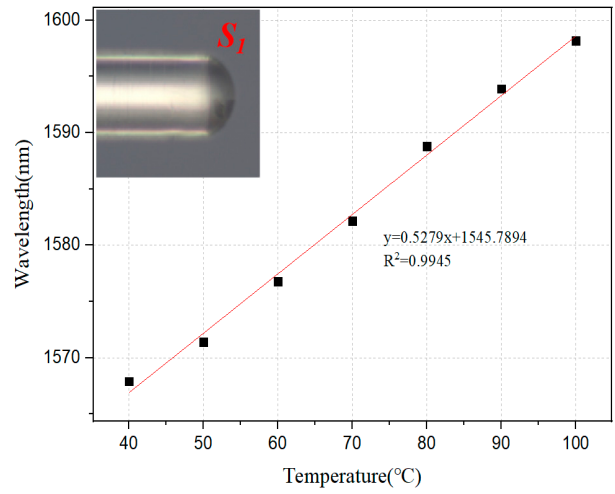


Figure 5. Temperature detection system.

As shown in Figure 6a, this clearly illustrates that the interference peaks exhibit a significant wavelength shift as temperature increases; Figure 6b displays the linear fitting analysis of temperature response. The experimental results show that the wavelength shift is about 30.25 nm and the consistency of the red shift is excellent. The temperature sensitivity of the sensor is about 528 pm/°C. As revealed in Figure 7a, the temperature response of  $S_2$  has multiple interference peaks and a significant red shift from 1525 to 1610 nm. According to the fitting results shown in Figure 7b, the temperature sensitivity of  $S_2$  is marginally improved compared to  $S_1$ . The wavelength shifts reach up to 32.96 nm, which clearly demonstrates relatively great fitness with a linear curve, and the calculated temperature sensitivity is approximately 540 pm/°C. Figure 8a shows the interference spectrum of  $S_3$ . The fitting result in Figure 8b demonstrates that the peak shift of the  $S_3$  is about 61.46 nm, and the temperature sensitivity reaches up to 1033pm/°C. Almost exactly twice the amount  $S_3$  was investigated for having high sensitivity.  $S_3$  has the broadest temperature response range and the highest temperature sensitivity in fabricated samples. This is due to the fact that temperature sensitivity mainly relies on the thermal expansion coefficient and thermo–optic coefficient of the diaphragms. Additionally, the spectra of the latter two are slightly similar to a single FP cavity. This is caused by the little differences of refractive indexes of the two diaphragms.

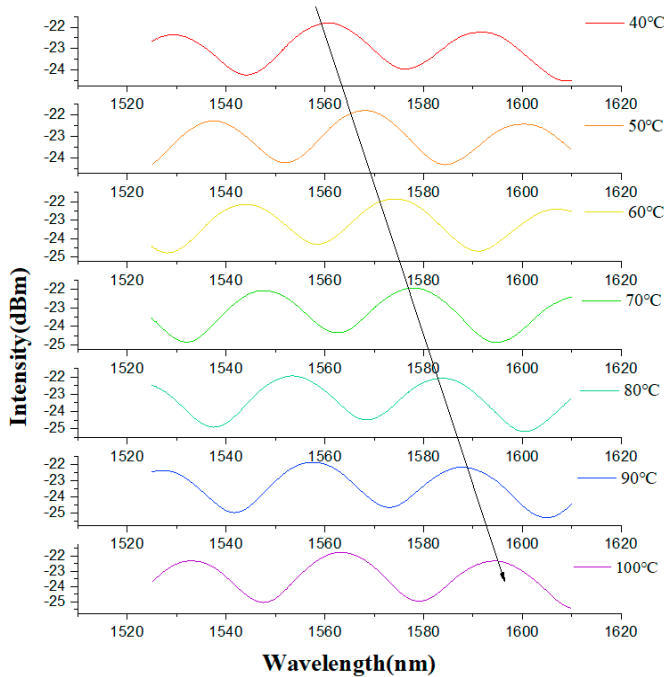


(a)

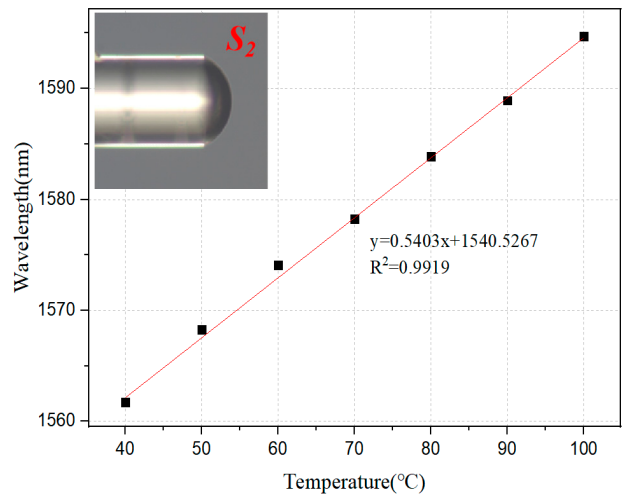


(b)

**Figure 6.** (a) The temperature (ranging from 40 to 100 °C, in strides of 10 °C) response interference spectrum of  $S_1$ (AB/PDMS); and (b) the temperature sensitivity of  $S_1$ .



(a)



(b)

**Figure 7.** (a) The temperature (ranging from 40 to 100 °C, in strides 10 °C) response interference spectrum of  $S_2$  (Ecoflex0030/PDMS); and (b) temperature sensitivity of  $S_2$ .

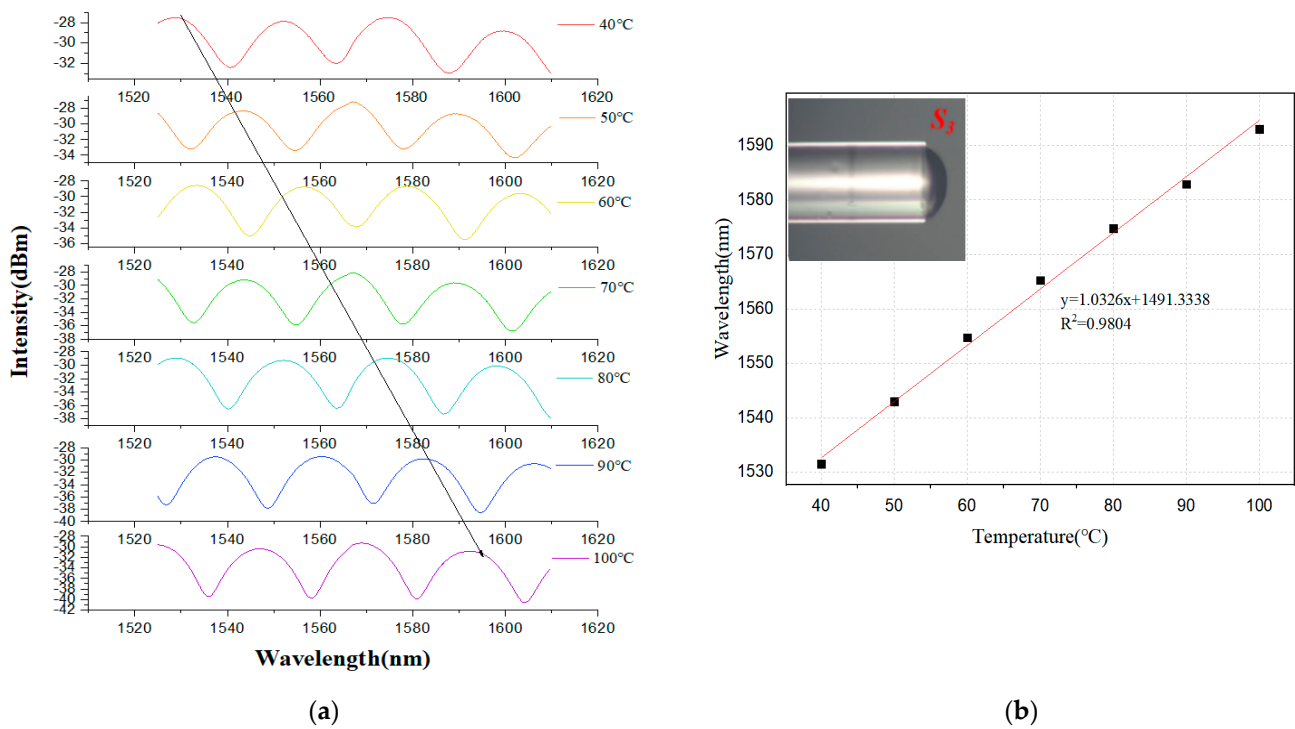


**Figure 8.** (a) The temperature (ranging from 40 to 100 °C, in strides of 10 °C) response interference Scheme 3. (PDMS/Ecoflex0030); and (b) temperature sensitivity of  $S_3$ .

### 3.2. Pressure Sensitivity Analysis

The schematic diagram of the pressure detection system is illustrated in Figure 9. The pressure test range is set from 100 to 400 kPa with increments of 10 kPa. The fabricated samples are placed in the air chamber and sealed with strong adhesive.

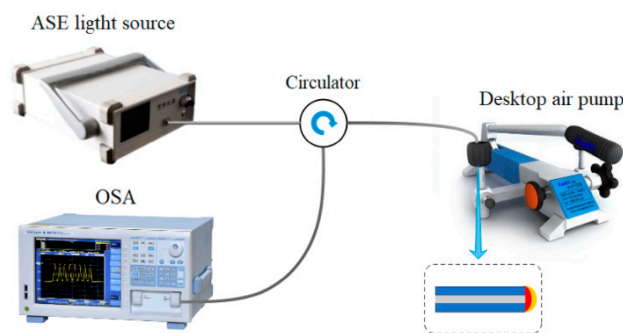


**Figure 9.** Pressure detection system.

Figure 10a displays that the interference spectrum of  $S_1$  has multiple prominent interference peaks over the detected wavelength range. The wavelength peaks increase as gas pressure increases. As described in Figure 10b, the peak shift is 4.78 nm and the fitting correlation coefficient  $R^2$  is about 0.998. The calculated pressure sensitivity is 16.0 pm/kPa. The low sensitivity found in  $S_1$  is due to the poor elastic effects. Figure 11a also shows the red shift of the spectra as pressure increases and the spectra present a consistent trend. In Figure 11b, the linear fitting result shows that the wavelength shift is about 10.48 nm, and the pressure sensitivity reaches up to 34.6 pm/kPa. More than twice the amount of  $S_2$  was fabricated having a high sensitivity to  $S_1$ . Figure 12a depicts that the  $S_3$  has a marginally lower pressure sensitivity compared to its high temperature sensitivity. According to Figure 12b, after linear fitting analysis, the wavelength shift and gas pressure sensitivity

are calculated to be 9.09 nm and 30.2 pm/kPa. The gas pressure sensitivity of the  $S_2$  was the best one among the fabricated samples. The sample  $S_2$ , which was provided with a wide measurement range, exhibits good response under high pressure.

As Table 3 shows, the performances of the proposed sensor and existing reports were concluded. The results demonstrate that the composite structures with dual FP cavities proposed in this paper possess moderate temperature and pressure sensitivity. However, we found that it is temporarily impossible to realize the simultaneous detection of the dual parameters due to the existing detection scheme and limited bandwidth of the used ASE light source. An ASE light source with a wider spectral range is needed to display more obvious three-beam interference peaks or valleys, and thus we can demodulate the high-frequency and low-frequency components to detect dual parameters simultaneously.

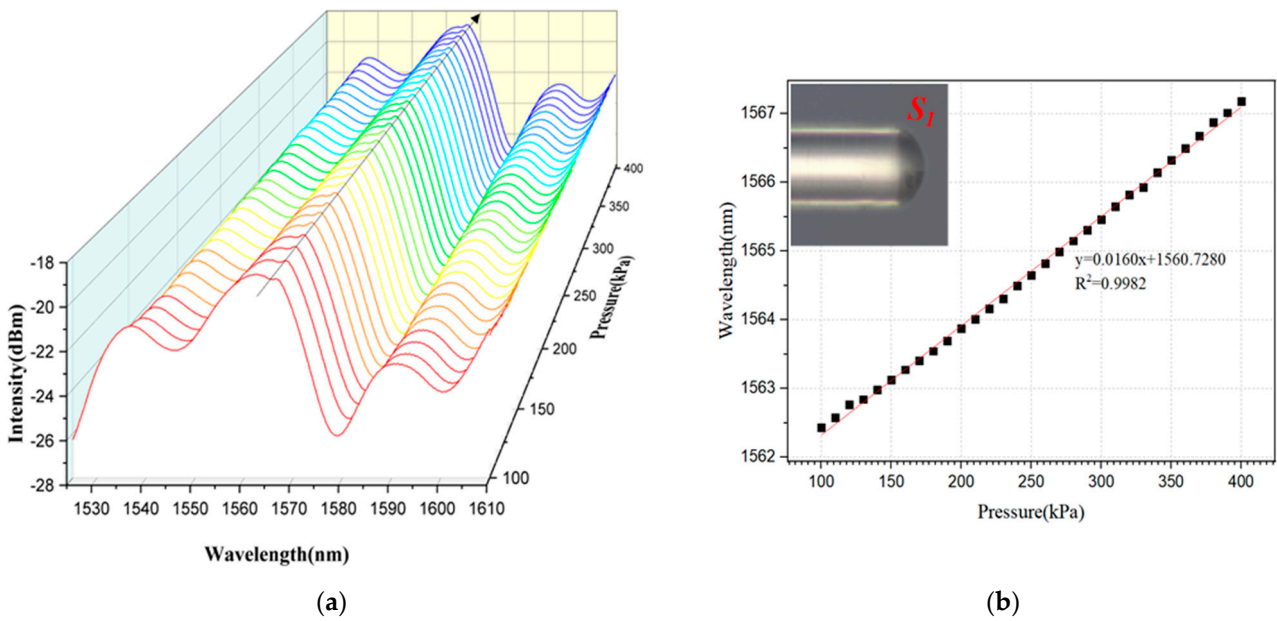


**Figure 10.** (a) The gas pressure (ranging from 100 to 400 kPa, in strides of 10 kPa) response interference spectrum of  $S_1$  (AB/PDMS); and (b) pressure sensitivity of  $S_1$ .

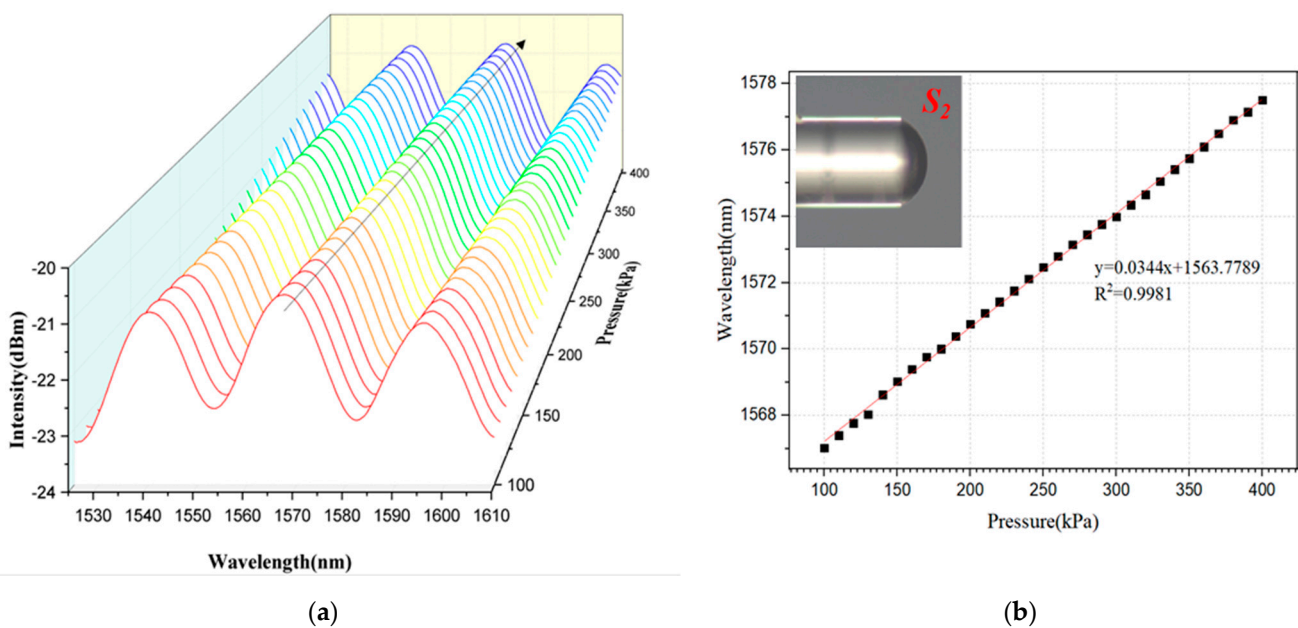


**Figure 11.** (a) The gas pressure (ranging from 100 to 400 kPa, in strides of 10 kPa) response interference spectrum of  $S_2$  (Ecoflex0030/PDMS); and (b) pressure sensitivity of  $S_2$ .

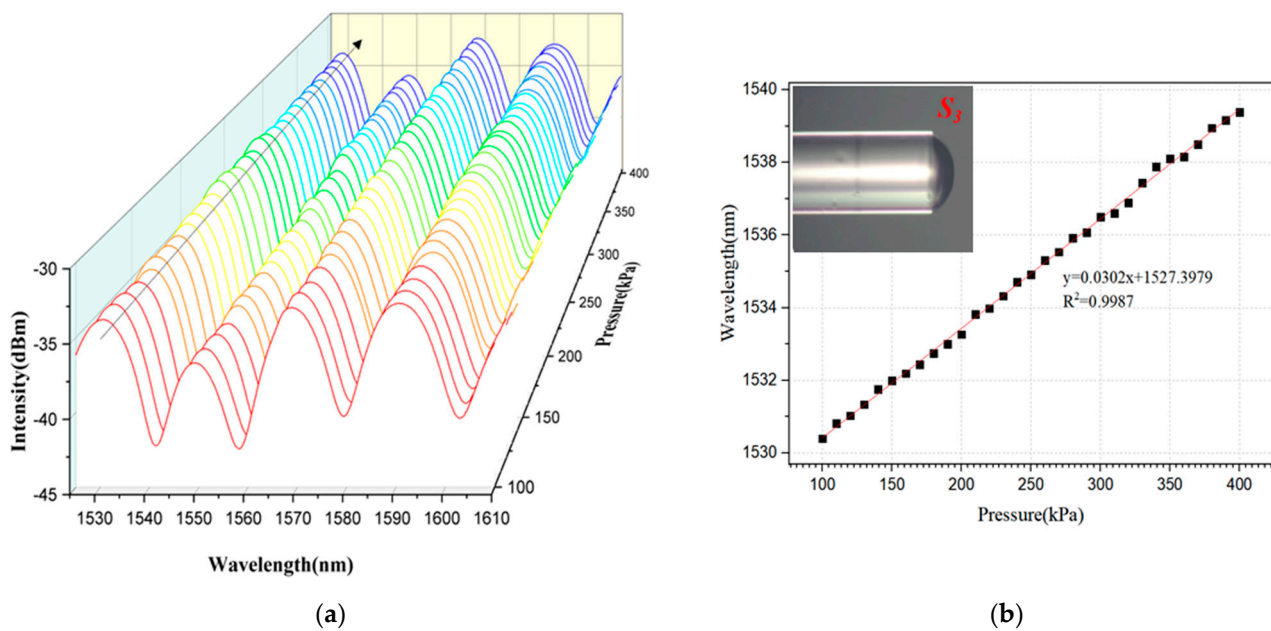


**Figure 12.** (a) The gas pressure (ranging from 100 to 400 kPa, in strides of 10 kPa) response interference spectrum of  $S_3$  (PDMS/Ecoflex0030); and (b) pressure sensitivity of  $S_3$ .

**Table 3.** Comparison for the performances of the proposed sensor and existing reports.

Sensor Structure	Temperature Sensitivity	Pressure Sensitivity	Simultaneous	Ref.
FBG cascade FPI	223.4 pm/°C	24.99 pm/kPa	Yes	2019 [5]
Hybrid Miniature FPI with Dual Optical Cavities	2.9 nm/°C	12.2nm/kPa	Yes	2014 [8]
SMF-SMF-HCF-CF	19.8nm/°C	98pm/kPa	Yes	2018 [9]
Dual-cavity FPI with Cascade Hollow-core Fibers	17 nm/°C	1.336 nm/kPa	No	2018 [11]
Hollow-Core Fiber-Based All-Fiber FPI	9.22 pm/°C	1.05 pm/kPa	Yes	2019 [13]
FBG incorporated FPI	0.871 pm/°C	4.071 pm/MPa	Yes	2016 [15]
FPI based on Pendant Polymer Droplet	249 pm/°C	1.130 pm/kPa	Yes	2015 [17]
FPI embedded with Microspheres	7.1 pm/°C	2.126 pm/kPa	Yes	2016 [18]
SMF-HCF-SMF	0.584 nm/°C	3.884 pm/kPa	No	2019 [30]
Diaphragm-Free Fiber-Optic FPI	14.8 pm/°C	4.28 pm/kPa	No	2018 [31]
FPI based on In-fiber Micro-cavity and Fiber-tip	0.0108 nm/°C	4.158 pm/kPa	Yes	2018 [32]
A Dual-Core Photonic Crystal Fiber Sensor	20.7 pm/°C	−3.47 pm/MPa	No	2011 [33]
Composite Structure with Dual FP Cavities	$S_1$ : 528 pm/°C $S_2$ : 540 pm/°C $S_3$ : 1033 pm/°C	$S_1$ : 16.0 pm/kPa $S_2$ : 34.6 pm/kPa $S_3$ : 30.2 pm/kPa	No	Our work

In addition, as Figures 13 and 14 show, this paper also set up another experiment to verify the repeatability and stability of the sensor. Figure 14 shows the repeatability and stability of the sensors by linearly fitting the peak shift in the heating and cooling experiment. Figure 14 displays that the peak shift error over the temperature range of 60–100 °C is caused by the residual temperature under the cooling process. The fitting curves show similar slopes and a high degree of coincidence. It was proven that the dual FP cavities structure has excellent recovery capability for the thermal expansion effect and thermo-optical effect.

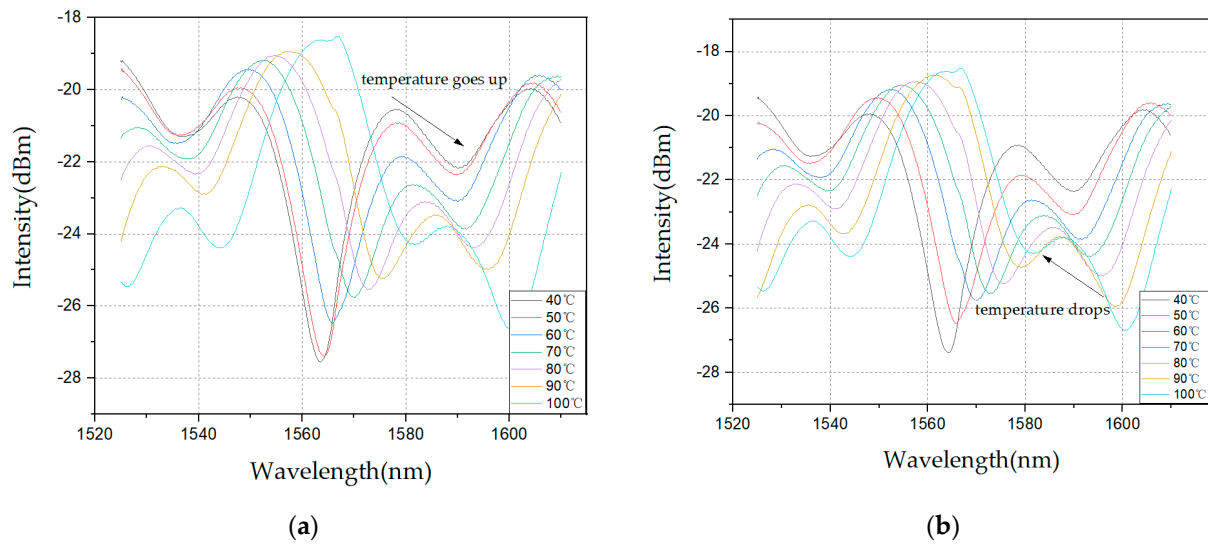


**Figure 13.** The performances for the repeatability and stability of the sensor: (a) the interference Scheme 40. to 100 °C; and (b) the interference spectrum with temperature drops from 100 to 40 °C.

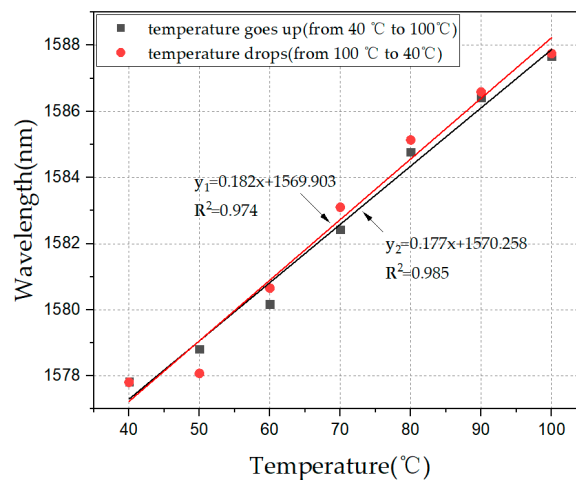


**Figure 14.** The sensitivity of the repeatability and stability of the sensor.

#### 4. Conclusions

In this paper, a novel composite structure composed of dual FP cavities for fiber sensing based on the multiple transfer method was proposed to measure the temperature and pressure, which possesses the advantages of proper sensitivity, simple fabrication, cost-effectiveness, and controllable cavity length. It was proven that the measured temperature or pressure sensitivity was closely related to the properties and combination modes of the diaphragms. According to the experimental results, by optimizing the combinations and parameters of dual-diaphragms, this study found that the temperature or pressure sensitivity can be adjusted over a certain range within the test temperature range of 40–100 °C and a pressure range of 100–400 kPa. This shows that the composite structure designed with dual FP cavities in this study has a proper sensitivity and can meet various sensitivity-demanding application scenarios.

**Author Contributions:** Conceptualization, J.W., L.L., S.L., D.W. and G.W.; methodology, J.W. and G.W.; formal analysis, J.W. and L.L.; writing—original draft preparation, J.W., L.L. and S.L.; writing—review and editing, J.W., L.L., S.L., W.W., M.S. and G.W.; visualization, J.W., W.W. and D.W.; and supervision, G.W. and M.H. All authors have read and agreed to the published version of the manuscript.

**Funding:** This research was funded by Hainan Key R&D Program (ZDYF2019115), the National Natural Science Foundation of China (Nos. 61865005 and 61762033), the Open Project Program of Wuhan National Laboratory for Optoelectronics (No. 2020WNLOKF001), the Natural Science Foundation of Hainan Province (2019CXTD400 and 617079), the National Key Technology Support Program (2015BAH55F04 and 2015BAH55F01), the Major Science and Technology Project of Hainan Province (ZDKJ2016015), and the Scientific Research Starting Foundation of Hainan University (KYQD(ZR)1882).

**Institutional Review Board Statement:** Not applicable.

**Informed Consent Statement:** Not applicable.

**Data Availability Statement:** The data that support the findings of this study are available from the corresponding author upon reasonable request.

**Acknowledgments:** We are very grateful to the relevant funds for their support of this paper.

**Conflicts of Interest:** The authors declare no conflict of interest.

## References

1. Yang, T.; He, X.; Ran, Z.; Xie, Z.; Rao, Y.; Qiao, X.; He, Z.; He, P. Highly Integrated All-Fiber FP/FBG Sensor for Accurate Measurement of Strain under High Temperature. *Materials* **2018**, *11*, 1867. [\[CrossRef\]](#)
2. Zawisza, R.; Eftimov, T.; Mikulic, P.; Bock, W.J.; Jaroszewicz, L.R. Ambient Refractive-Index Measurement with Simultaneous Temperature Monitoring Based on a Dual-Resonance Long-Period Grating Inside a Fiber Loop Mirror Structure. *Sensors* **2018**, *18*, 2370. [\[CrossRef\]](#)
3. Liu, B.; Luo, J.; Liu, S.; Chen, Y.; Huang, B.; Liao, C.; Wang, Y. A Probe-Shaped Sensor With FBG and Fiber-Tip Bubble for Pressure and Temperature Sensing. *Photonics Sens.* **2021**, 1–7. [\[CrossRef\]](#)
4. Wang, Y.; Yang, M.; Wang, D.N.; Liu, S.; Lu, P. Fiber in-line Mach-Zehnder interferometer fabricated by femtosecond laser micromachining for refractive index measurement with high sensitivity. *J. Opt. Soc. Am. B* **2010**, *27*, 370–374. [\[CrossRef\]](#)
5. Liu, Y.; Yang, D.; Wang, Y.; Zhang, T.; Shao, M.; Yu, D.; Fu, H.; Jia, Z. Fabrication of dual-parameter fiber-optic sensor by cascading FBG with FPI for simultaneous measurement of temperature and gas pressure. *Opt. Commun.* **2019**, *443*, 166–171. [\[CrossRef\]](#)
6. Monfared, Y.E.; Liang, C.; Khosravi, R.; Kacerovska, B.; Yang, S. Selectively toluene-filled photonic crystal fiber Sagnac interferometer with high sensitivity for temperature sensing applications. *Results Phys.* **2019**, *13*, 102297. [\[CrossRef\]](#)
7. Yin, J.; Liu, T.; Jiang, J.; Liu, K.; Wang, S.; Qin, Z.; Zou, S. Batch-Productible Fiber-Optic Fabry–Pérot Sensor for Simultaneous Pressure and Temperature Sensing. *IEEE Photonics Technol. Lett.* **2014**, *26*, 2070–2073. [\[CrossRef\]](#)
8. Bae, H.; Yun, D.; Liu, H.; Olson, D.A.; Yu, M. Hybrid Miniature Fabry–Pérot Sensor with Dual Optical Cavities for Simultaneous Pressure and Temperature Measurements. *J. Lightwave Technol.* **2014**, *32*, 1585–1593. [\[CrossRef\]](#)
9. Gao, H.; Jiang, Y.; Cui, Y.; Zhang, L.; Jia, J.; Hu, J. Dual-Cavity Fabry–Pérot Interferometric Sensors for the Simultaneous Measurement of High Temperature and High Pressure. *IEEE Sens. J.* **2018**, *18*, 10028–10033. [\[CrossRef\]](#)
10. Zhang, L.; Jiang, Y.; Gao, H.; Jia, J.; Cui, Y.; Wang, S.; Hu, J. Simultaneous Measurements of Temperature and Pressure With a Dual-Cavity Fabry–Pérot Sensor. *IEEE Photonics Technol. Lett.* **2018**, *31*, 106–109. [\[CrossRef\]](#)
11. Chen, M.-Q.; Zhao, Y.; Xia, F.; Peng, Y.; Tong, R.-J. High sensitivity temperature sensor based on fiber air-microbubble Fabry–Pérot interferometer with PDMS-filled hollow-core fiber. *Sens. Actuators A Phys.* **2018**, *275*, 60–66. [\[CrossRef\]](#)
12. Bai, Y.; Qi, Y.; Dong, Y.; Jian, S. Highly Sensitive Temperature and Pressure Sensor Based on Fabry–Pérot Interference. *IEEE Photonics Technol. Lett.* **2016**, *28*, 2471–2474. [\[CrossRef\]](#)
13. Liu, Y.; Wang, Y.; Yang, D.; Wu, J.; Zhang, T.; Yu, D.; Zhenan, J.; Fu, H.; Jia, Z. Hollow-Core Fiber-Based All-Fiber FPI Sensor for Simultaneous Measurement of Air Pressure and Temperature. *IEEE Sens. J.* **2019**, *19*, 11236–11241. [\[CrossRef\]](#)
14. Pevec, S.; Donlagic, D. Miniature all-fiber Fabry–Pérot sensor for simultaneous measurement of pressure and temperature. *Appl. Opt.* **2012**, *51*, 4536–4541. [\[CrossRef\]](#) [\[PubMed\]](#)
15. Wu, S.; Yan, G.; Wang, C.; Lian, Z.; Chen, X.; He, S. FBG Incorporated Side-open Fabry–Pérot Cavity for Simultaneous Gas Pressure and Temperature Measurements. *J. Lightwave Technol.* **2016**, *34*, 1. [\[CrossRef\]](#)
16. Zhang, W.; Zhuang, W.; Dong, M.; Zhu, L.; Meng, F. Dual-Parameter Optical Fiber Sensor for Temperature and Pressure Discrimination Featuring Cascaded Tapered-FBG and Ball-EFPI. *IEEE Sens. J.* **2019**, *19*, 5645–5652. [\[CrossRef\]](#)
17. Sun, B.; Wang, Y.; Qu, J.; Liao, C.; Yin, G.; He, J.; Zhou, J.; Tang, J.; Liu, S.; Li, Z.; et al. Simultaneous measurement of pressure and temperature by employing Fabry–Pérot interferometer based on pendant polymer droplet. *Opt. Express* **2015**, *23*, 1906–1911. [\[CrossRef\]](#)
18. Xu, B.; Liu, Y.M.; Wang, D.N.; Li, J.Q. Fiber Fabry–Pérot Interferometer for Measurement of Gas Pressure and Temperature. *J. Lightwave Technol.* **2016**, *34*, 4920–4925. [\[CrossRef\]](#)
19. Fu, D.; Liu, X.; Shang, J.; Sun, W.; Liu, Y. A Simple, Highly Sensitive Fiber Sensor for Simultaneous Measurement of Pressure and Temperature. *IEEE Photonics Technol. Lett.* **2020**, *32*, 747–750. [\[CrossRef\]](#)

20. Ge, M.; Li, Y.; Han, Y.; Xia, Z.; Guo, Z.; Gao, J.; Qu, S. High-sensitivity double-parameter sensor based on the fibre-tip Fabry–Pérot interferometer. *J. Mod. Opt.* **2016**, *64*, 1–5. [[CrossRef](#)]
21. Kangpeng, Z.; Wei, H.; Wen, Z.; Mingli, D.; Lianqing, Z. A Dual-parameter Fabry–Perot Interferometer Sensor Based on Single Mode-Photonic Crystal-Multimode Fiber Structure. *Instrum. Exp. Tech.* **2019**, *62*, 426–431. [[CrossRef](#)]
22. Liu, X.; Gang, T.; Tong, R.; Qiao, X.; Zuo, C.; Bai, X.; Bian, C.; Hu, M. Air-coupled fiber Fabry-Perot ultrasonic sensor formed by diaphragm for seismic physical model imaging. *Optik* **2018**, *168*, 794–799. [[CrossRef](#)]
23. Kanawade, R.; Kumar, A.; Pawar, D.; Vairagi, K.; Late, D.; Sarkar, S.; Sinha, R.K.; Mondal, S. Negative axicon tip-based fiber optic interferometer cavity sensor for volatile gas sensing. *Opt. Express* **2019**, *27*, 7277–7290. [[CrossRef](#)] [[PubMed](#)]
24. Park, C.-S.; Joo, K.-I.; Kang, S.-W.; Kim, H.-R. A PDMS-Coated Optical Fiber Bragg Grating Sensor for Enhancing Temperature Sensitivity. *J. Opt. Soc. Korea* **2011**, *15*, 329–334. [[CrossRef](#)]
25. Yu, T. Study on Mechanical Properties and Bonding of PDMS in Flexible Electronics. Master’s Thesis, Yangzhou University, Yangzhou, China, 2017.
26. Ren, X.; Chen, J.; Xu, F.; Nie, M. Study on Bilayer-Microstructure Flexible Strain Sensors Based on Carbon Nanotubes. *Chin. J. Sens. Actuators* **2019**, *32*, 654–657.
27. Zhang, Z.; Ping, Z.; Peng, L.; Sun, F. Thermo-optic coefficients of polymers for optical waveguide applications. *Polymer* **2006**, *47*, 4893–4896. [[CrossRef](#)]
28. Li, J.; Gai, L.; Li, H.; Hu, H. A high sensitivity temperature sensor based on packaged microfiber knot resonator. *Sens. Actuators A Phys.* **2017**, *263*, 369–372. [[CrossRef](#)]
29. Zhou, W.; Li, Y. Modeling and Analysis of Soft Pneumatic Actuator with Symmetrical Chambers Used for Bionic Robotic Fish. *Soft Robot.* **2020**, *7*, 168–178. [[CrossRef](#)]
30. Gao, H.; Jiang, Y.; Zhang, L.; Cui, Y.; Jiang, Y.; Jia, J.; Jiang, L. Antiresonant mechanism based self-temperature-calibrated fiber optic Fabry–Perot gas pressure sensors. *Opt. Express* **2019**, *27*, 22181–22189. [[CrossRef](#)] [[PubMed](#)]
31. Liang, H.; Jia, P.; Liu, J.; Fang, G.; Li, Z.; Hong, Y.-P.; Liang, T.; Xiong, J. Diaphragm-Free Fiber-Optic Fabry-Perot Interferometric Gas Pressure Sensor for High Temperature Application. *Sensors* **2018**, *18*, 1011. [[CrossRef](#)]
32. Liu, Y.; Zhang, T.; Wang, Y.; Yang, D.; Liu, X.; Fu, H.; Jia, Z. Simultaneous measurement of gas pressure and temperature with integrated optical fiber FPI sensor based on in-fiber micro-cavity and fiber-tip. *Opt. Fiber Technol.* **2018**, *46*, 77–82. [[CrossRef](#)]
33. Chen, D.; Hu, G.; Chen, L. Pressure/Temperature Sensor Based on a Dual-Core Photonic Crystal Fiber. In Proceedings of the Asia Communications & Photonics Conference & Exhibition. International Society for Optics and Photonics, Shanghai, China, 14 November 2011. [[CrossRef](#)]